Numerical Simulation of the VAR Process with calco*soft*®-2D and its Validation

G. Reiter[a], V. Maronnier[b], C. Sommitsch[a], M. Gäumann[b], W. Schützenhöfer[a], R. Schneider[a]

[a] Böhler Edelstahl GmbH & Co KG, 8605 Kapfenberg, Austria
[b] Calcom SA, 1015 Lausanne, Switzerland

Abstract
The numerical simulation of remelting processes has become more and more popular over the last 2 decades. The reasons for the increasing interest of both universities and industry are obvious: to get a better understanding of the processes and thus to optimise them. Böhler Edelstahl GmbH & Co KG has been using the commercially available calco*soft*®-2D software to simulate the vacuum arc remelting (VAR) process for the last 2 years.
The calco*soft*®-2D software is FEM based and solves the heat flow equation in 2-dimensional systems. Convection and heat transport are accounted for by coupling the heat conduction equation with the Navier-Stokes equation. For the numerical simulation of the VAR process, a special module has been developed in calco*soft*®-2D which takes into account the magneto-hydrodynamic effects caused by the high current density in the liquid pool region and their influence on the pool flow regimes that occur.
Practical experiments were carried out on ingots made of Alloy 718. Pool profiles were investigated at different melt rates on 410mm (16") and 510mm (20") diameter ingots. Additionally, inverse calculations were carried out to obtain the heat flow boundary conditions required for the simulation.
An understanding of the heat balance of the system forms the basis of the remelting simulations. Calculations and estimations of the boundary conditions including the heat fluxes, the shrinkage gap formation and the additional heat due to arc radiation are described. Simulations were carried out to calculate heat flow, transport and fluid flow problems.
The influence of the magneto-hydrodynamic effect on the fluid flow, the comparison of simulation and experimental results, and the dependence of the remelting process on different ingot dimensions are discussed.

1 INTRODUCTION

During the last 50 years the VAR-process has become a standard remelting facility for the production of special alloys [1]. Böhler Edelstahl GmbH & Co KG operates 3 VAR-furnaces capable of producing ingots up to 950mm in diameter, and which are mainly used for the production of special steels and nickel-based alloys. To meet the demands made of these alloys, a very high level of understanding of the process is necessary, which can be extended with the aid of solidification simulation. A project was started with the aim of simulating the VAR process using the commercially available calco*soft*®-2D software and to develop this software further for this application.
The difficulties involved in simulating VAR processes are directly linked to the wide range of physical and chemical phenomena which occur simultaneously and are often coupled in such remelting processes [2]. A comprehensive numerical simulation would incorporate fluid flow, heat and mass transfer, electromagnetic effects, solidification (including microstructure prediction) and macro-segregation. The modeling of heat transfer, fluid flow, solidification including grain structure prediction, solid-state transformation, hot tears, porosity and macro-segregation is already done in the commercial finite element software calco*soft*®-2D [3] dedicated to casting processes. Moreover, the software calco*soft*®-2D also includes an induction heating model which allows magnetic stirring to be modeled. However, due to the geometry of the VAR furnace and its power supply, a new axisymmetric electromagnetic solver which takes into account both Lorentz's forces and Ohm's law heating, has been developed in calco*soft*®-2D to simulate the VAR process.

2 THE MATHEMATICAL MODEL

The model is based on the numerical solutions of the Navier-Stokes, Fourier and steady-state Maxwell equations. Heat and fluid flow models are detailed in [3]. The electromagnetic model is different to that used by the authors of [4,5,6,7]. First, the electric potential and the electric current density are computed as given in [8] but taking the influence of the velocity into account. Then, the magnetic field is computed from an original model [9]. Finally, the Lorentz's forces and Ohm's law heating can be evaluated.

The following assumptions are made: the ingot is treated as axisymmetric, and modelled in two dimensions using cylindrical coordinates, figure 1; the arc, created by the circulation of a direct current between the cathode and the mould, is assumed to be diffuse, i.e. without short-circuit; a stationary regime is assumed in the simulations. In accordance with these assumptions, only the upper part of the ingot is simulated. The remained of the ingot is taken into account by assuming that material disappears at the lower boundary of the geometry simulated. Appropriate boundary conditions are applied to represent the arc and mass transfer from the cathode. The equations solved are listed below.

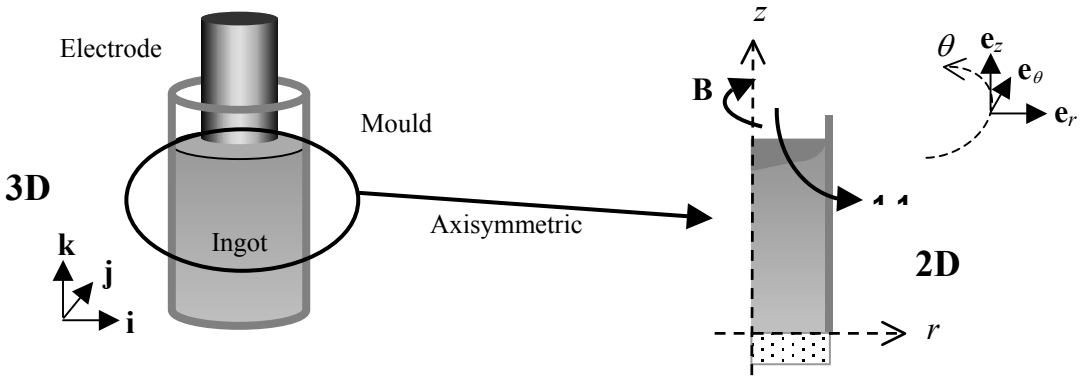

Fig. 1: Axisymmetric situation of the VAR process.

2.1 Energy conservation

The energy equation to be solved is:

$$\frac{\partial H}{\partial t} + \mathbf{v}_s \cdot \nabla H + \rho c_p (\mathbf{v} - \mathbf{v}_s) \cdot \nabla T - \operatorname{div}(\kappa \cdot \nabla T) = \frac{\mathbf{J} \cdot \mathbf{J}}{\sigma}, \tag{1}$$

where H is the volumetric enthalpy, $\mathbf{v}_s$ is the transport velocity of the solid, ρ the density, c_p the specific heat, κ the thermal conductivity and T the temperature. The average velocity $\mathbf{v}$ is defined by $\mathbf{v} = f_s \mathbf{v}_s + f_l \mathbf{v}_l$, where f_s is the fraction of solid, f_l the fraction of liquid and $\mathbf{v}_l$ the velocity of the fluid. The right hand side of the equation represents the Ohm's law heating, where σ is the electrical conductivity and $\mathbf{J}$ the electric current density. Furthermore, the conversion into variation of temperature and volume fraction is made according to a microscopic model of solidification.

2.2 Continuity and momentum equations

Incompressible Newtonian viscous fluids are assumed. The mass conservation is:

$$\operatorname{div} \mathbf{v} = 0. \tag{2}$$

Taking into account the interaction between the solid phase and the liquid phase in the mushy zone and using the Boussinesq approximation, the momentum equation can be written as follows:

$$\rho \frac{\partial \mathbf{v}}{\partial t} + \frac{\rho}{f_l}(\mathbf{v} \cdot \nabla)\mathbf{v} - 2\mu \operatorname{div}(\varepsilon(\mathbf{v})) + f_l \nabla p = f_l \rho \mathbf{g} \beta (T - T_0) + f_l \, \mathbf{J} \times \mathbf{B} - f_l \frac{\mu}{K}(\mathbf{v} - \mathbf{v}_s), \tag{3}$$

where p is the pressure of the fluid, μ the viscosity, $\mathbf{g}$ the gravitational acceleration, β the thermal expansion coefficient and T_0 a reference temperature. The term $\varepsilon(\mathbf{v})$ corresponds to the rate of deformation tensor. The term $\mathbf{J} \times \mathbf{B}$, where $\mathbf{B}$ is the magnetic induction field, represents the Lorentz's forces and the last term on the right hand side represents the damping of the fluid in the mushy region due to the solid, where K is the local permeability of the mushy region. In the liquid, the permeability is infinite and the source term vanishes.

2.3 Electromagnetic model

A quasi steady-state electromagnetic model has to be computed for each time step. The circulation of a direct electric current between the cathode and the mould creates a magnetic field which must satisfy the following steady-state Maxwell's equations in the whole space:

$$\mathbf{rot}\, \mathbf{B} = \mu_0 \mathbf{J}, \tag{4}$$

$$\mathbf{rot}\, \mathbf{E} = 0 \Rightarrow \mathbf{E} = -\nabla \varphi, \tag{5}$$

$$\operatorname{div} \mathbf{B} = 0, \tag{6}$$

where μ_0 is the magnetic permeability, φ the electric potential and **E** the electric field. Moreover, Ohm's law is applied in the set of conductors:

$$\mathbf{J} = \sigma \left(\mathbf{E} + \mathbf{v} \times \mathbf{B}\right). \tag{7}$$

First, values of electric potential φ are computed in solving the electric current conservation equation, obtained in combining equations (5) and (7) and setting the divergence of **J** equal to zero, that is

$$-\text{div}\ (\sigma \nabla \varphi) = -\text{div}\ (\sigma\, \mathbf{v} \times \mathbf{B}). \tag{8}$$

Second, applying Ohm's law with the previous value of the electric potential, the electric current density can then be computed as follows:

$$\mathbf{J} = \sigma \left(\text{-}\nabla \varphi + \mathbf{v} \times \mathbf{B}\right). \tag{9}$$

Finally, according to the first assumption, the magnetic induction is defined by $\mathbf{B} = B_\theta(r,z)\,\mathbf{e}_\theta$, automatically satisfying equation (6). As B_θ is bounded inside a conductor, it is possible to define B_θ explicitly from the relationship described in (4), as it is in [4]. However, the magnetic field is computed in the following way: B_θ fulfils equation (4) in cylindrical coordinates, that is:

$$\frac{\partial}{\partial r}(rB_\theta) = \mu_0 r J_z \quad \text{and} \quad \frac{\partial}{\partial z} B_\theta = -\mu_0 J_r, \tag{10}$$

where J_z and J_r are the components of **J** according to $\mathbf{e}_r$ and $\mathbf{e}_z$. Defining $\psi = rB_\theta$, these equations represent the components of the gradient of ψ according to *r* and *z*. Taking the divergence of the gradient of ψ, with *r* and *z* as Cartesian coordinates yields:

$$\Delta_{rz}\,\psi = \text{div}\,\mathbf{f} = \text{div}\begin{bmatrix} \mu_0 r J_z \\ -\mu_0 r J_r \end{bmatrix}. \tag{11}$$

Using values of **J** calculated in (9), we compute ψ and then B_θ in solving equation (11), with the following boundary conditions to have a well-posed problem: $\psi = 0$ at the axis of symmetry and the natural condition $\nabla_{rz}\,\psi \cdot \mathbf{n} = \mathbf{f} \cdot \mathbf{n}$, otherwise, where **n** is the outward normal of the boundary.

Equations (1) for heat, (2)-(3) for fluid and (8) for electric potential require appropriate initial and boundary conditions.

3 CALCULATIONS

The VAR process is characterised by an axisymmetric geometry, so all calculations are carried out in a 2D axisymmetric system. The model used in the simulation contains the ingot and the copper mould; the electrode and the electric arc are not directly considered. Heat flow, transport of the solid phase, fluid flow and the magneto-dynamic effects in the pool due to the melt current are taken into account by the calculations.

Trials were carried out for two different dimensions, a 410mm (16") and a 510mm (20") diameter ingot, both made of Alloy 718. Geometry (mould and electrode dimension) and process parameters (melt rate and melt current) correlate to those used for industrial production. An adequately fine mesh was used with an increasing number of elements near to the top and at the ingot-mould interface.

Starting from fictitious start conditions, where the temperature of the whole ingot is set to 1300°C and the mould temperature is set to 36°C, the heat balance of the system is calculated until stationary conditions are reached. Hence, a sufficiently high number of time steps must be calculated. Transient process phases (e.g. changes in the melt rate or the falling in of material) and phases of the process which are transient by nature (e.g. hot topping or the start phase), are not taken into consideration.

3.1 Thermal model of the ingot

The thermal boundary conditions play an important part in the prediction of the temperature distribution and the pool profile during the steady-state phase of the VAR process. Figure 2 shows the heat fluxes during remelting, where heat flux 1 represents the incoming energy, heat flux 2 is based on radiation from the annulus to the mould, heat flux 3 stands for the heat transfer from the ingot to the cooling water and heat fluxes 4 and 5 represent the radiation from the electrode and the arc, respectively, to the mould [10,11]. The following main assumptions are made in the numerical model:

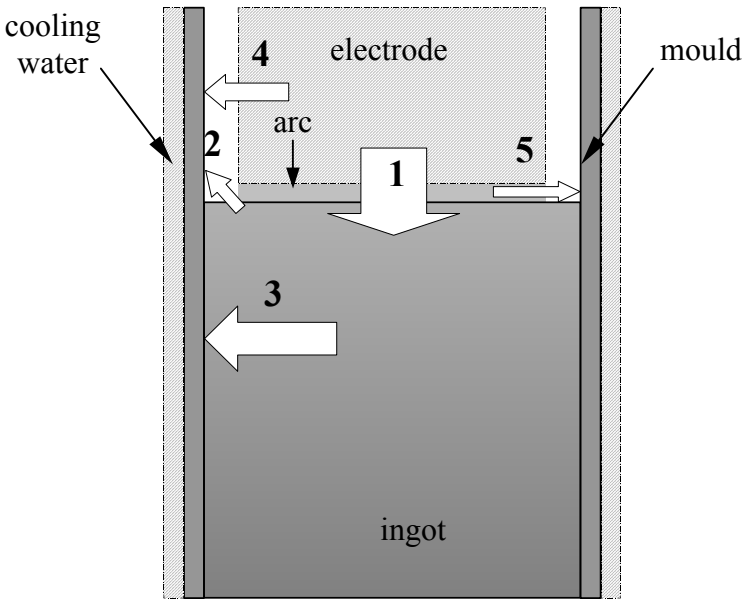

Figure 2: Heat fluxes during remelting

3.1.1 Heat flux 1

The total incoming energy, which consists of the energy of the droplets and the energy coming from the radiation of the electric arc, is represented by a constant temperature at the pool surface -- given by the liquidus temperature and superheat -- and a constant flow of material according to the melt rate. The superheat is estimated by multiplying the fraction of arc energy that goes into the melt by the power of the arc per electrode cross-section.

3.1.2 Heat flux 2

Different fill ratios lead to different annuli between the electrode and the mould. The heat transition at the annulus is governed by an arbitrarily set constant temperature.

3.1.3 Heat flux 3

A small contact zone can be distinguished from a gap between the solidified ingot and the mould due to shrinkage [12]. The critical temperature of gap formation was set to a temperature T_{crit} below the solidus temperature. Heat transfer h between the ingot and the mould was calculated by:

$$\begin{aligned} h &= h_{cont} \quad \text{if } T > T_{crit} \\ h &= h_r + h_g \quad \text{else} \end{aligned} \tag{12}$$

where h_{cont} is the heat transfer coefficient in the case of contact,

$$h_r = \varepsilon \sigma \frac{T^4 - T_m^4}{T - T_m} \tag{13}$$

is the heat transfer coefficient due to radiation, T is the temperature of the ingot surface, T_m is the temperature of the mould (inside), ε is the emissivity of the material and σ is the Stefan-Boltzman constant.

$$h_g = \frac{\lambda_g}{r_i \left[\ln\left(\frac{r_m}{r_i}\right) + \frac{g_i}{r_i} + \frac{g_m}{r_m} \right]} \tag{14}$$

is the conductive heat transfer coefficient using the analogy of conduction through the rarefied gas between coaxial cylinders which is valid for very low pressures [13], where λ_g denotes the thermal conductivity of gas, r the radius and g the temperature jump distance of the mould (subscript m) and the ingot (subscript i), respectively. For sufficiently large gaps, h_g can be approximated by λ_g/gap. This allows the presence of gas, e.g. He, in the shrinkage gap to be taken into consideration.

The heat transfer in the copper mould h_m is given by the thermal conductivity divided by the thickness of the mould.
The heat transfer between the mould and the cooling water h_w is based on the analogy of the heat transfer coefficient for turbulent flow in an annular tube [14]

$$\mathrm{St}\left(\mathrm{Pr}\right)^{\frac{2}{3}} = 0.023\left(\mathrm{Re}\right)^{-0.2}, \tag{15}$$

which depends on the Stanton number *St*, the Prandtl number *Pr* and the Reynolds number *Re*.
Thus, the overall heat transfer coefficient *h* between the ingot and the cooling water can be derived by:

$$h = \frac{1}{\frac{1}{h} + \frac{1}{h_m} + \frac{1}{h_w}}. \tag{16}$$

Figure 3 shows the dependence of the overall heat transfer coefficient, and its components, on the gap width. At small gap widths the heat transfers between the ingot and the mould and between the mould and the cooling water are of the same order of magnitude. For gap widths larger than 1mm only the heat transfer between mould and ingot is of major influence. The constant overall heat transfer coefficient in the case of contact is also shown in the figure.

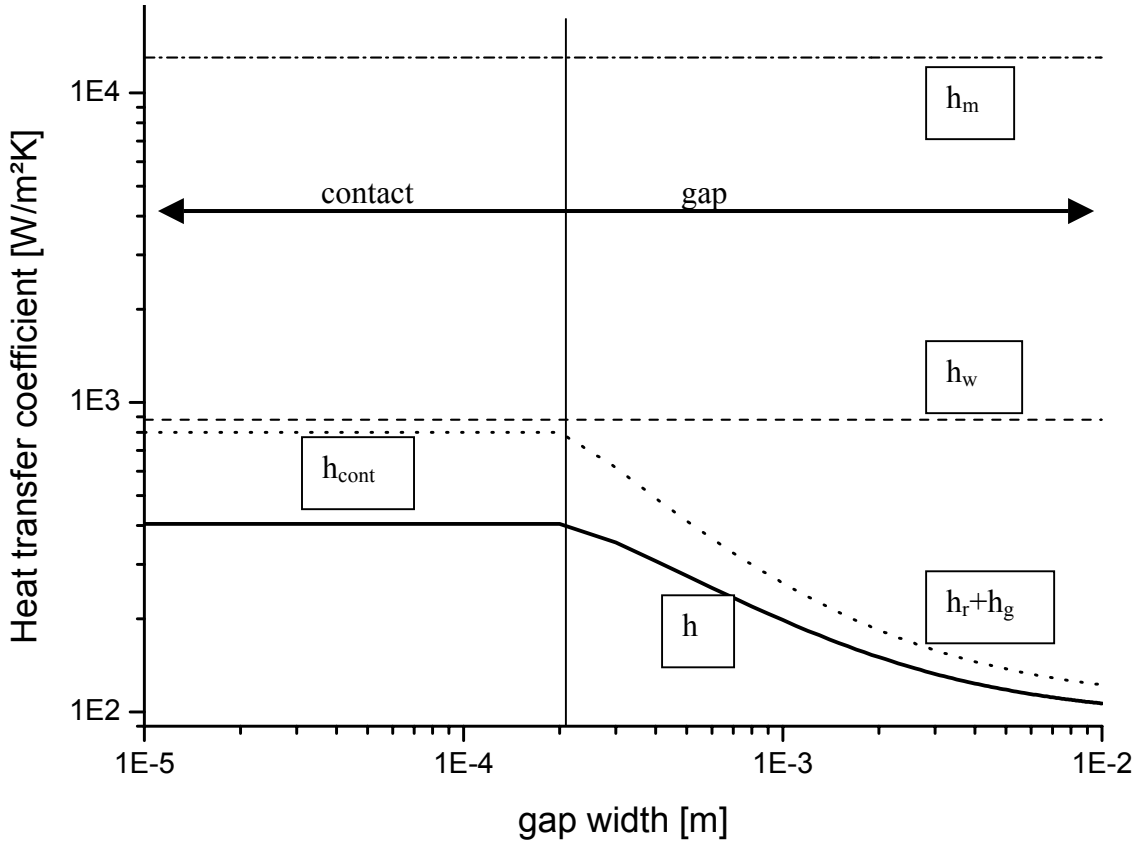

Figure 3: heat transfer coefficients between the ingot and the cooling water as a function of the gap width for Alloy 718: ingot diameter = 510mm, He pressure = 15Torr, temperature = 1273K. The transition from contact to gap was set to 0.2mm for this calculation.

To estimate the gap width, additional calculations were made using the FEM-code DEFORM™. This programme was developed for the calculation of metal forming processes, thus the liquid pool of the VAR cannot be described. Therefore the axisymmetric model was simplified in the following way: The real shape of the liquid pool formed, which is measured on a macro-etched longitudinal test specimen, gives the geometry of the ingot top. A fixed temperature - the solidus temperature - was chosen as the thermal boundary condition. Furthermore, the heat transfer between the ingot and the water cooled copper plate at the bottom was set to 800W/m²K.
The heat transfer between the ingot and the copper mould was modelled as follows: there is a contact boundary condition at the top, where the ingot touches the mould. In the case of contact there is a friction coefficient equal

to 0.3 and the heat transfer coefficient was set to 800W/m²K. This heat transfer coefficient was calculated by inverse modelling. After gap formation, the heat transfer consists of radiation and heat conduction by helium, which fills the gap. An emissivity of 0.4 and a constant heat transfer coefficient of 100 W/m^{2}K were chosen for this calculation.
The whole length profile of the gap was calculated as described above. Figure 3 depicts the result with an ingot height fixed at 2 meters. It shows the gap as a function of the vertical distance from the liquid pool. The gap opens very quickly in the first 500 mm below the pool. This follows from high temperature gradients in the vertical as well as in the radial direction. Further below, the temperature gradient of the ingot is very low therefore the ongoing thermal shrinkage which causes the gap formation is very slow. The maximum gap of the 510 mm ingot is around 4.5mm.

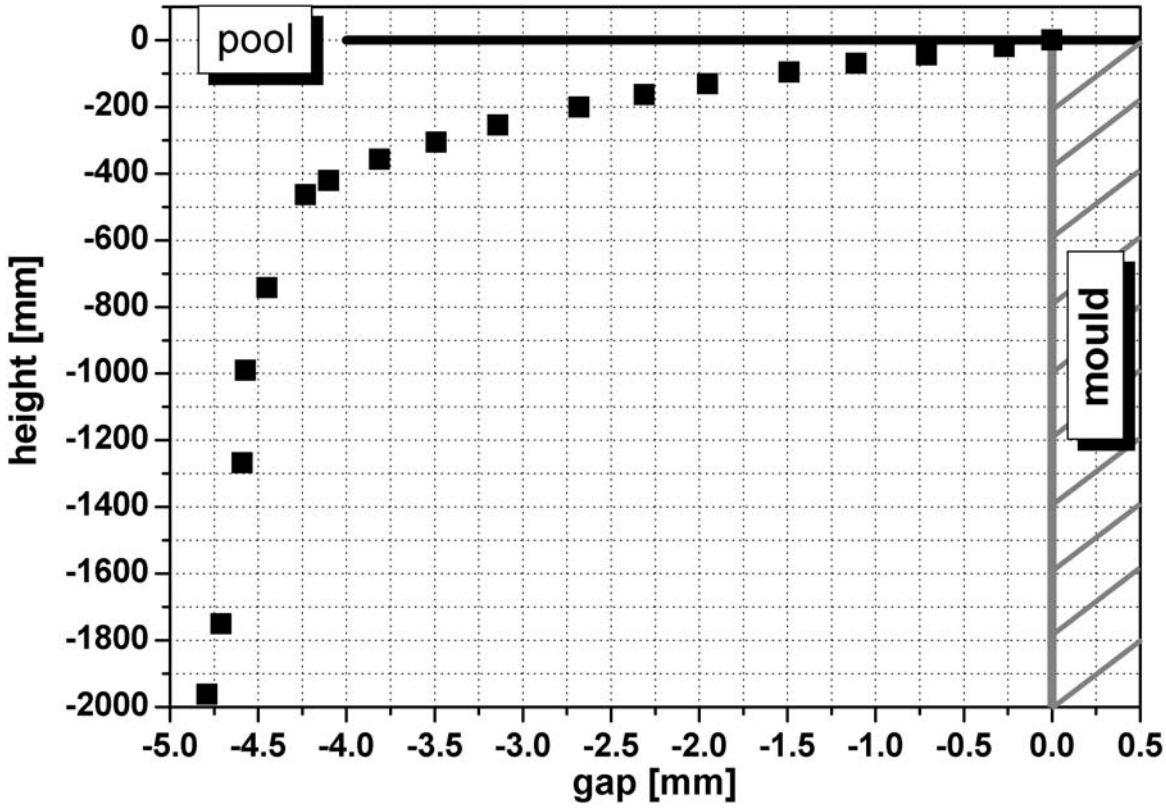

Figure 3: shrinkage gap formation as a function of distance from the liquid pool

3.1.4 Heat fluxes 4 and 5

In addition to that mentioned above, heat fluxes appear which have no direct influence on the ingot. Radiation occurs from the electric arc and the electrode directly to the mould.

3.2 Material data

All material data for Alloy 718 and for the mould material (copper) are taken from published databases [15].

4 RESULTS

4.1 Simulation results

The main results that are obtained are the temperature distribution, the distribution of the fraction of solid in the ingot and the fluid flow in the liquid pool. Figure 4 shows the simulation results for a 510mm ingot. The temperature distribution (figure 4 (a)) shows a superheated layer on the pool surface right below the electrode and a very steep gradient near to the mould in the upper region of the ingot. The fraction of solid distribution (figure 3 (b)) in principal shows a pool profile typical of a VAR ingot. The liquidus and solidus lines are set at a fraction of solid of 0.98 and 0.02 respectively. Almost no solid shelf is formed at the upper right corner of the ingot.
The magnification of the pool region illustrates the fluid flow in the liquid phase (figure 3 (c)). Two different flow regimes are visible: one swirl in the upper pool region near to the pool surface that is characterised by a

downwards flow in the centre of the ingot, and a second in the lower region where the fluid flows upwards at the centre.

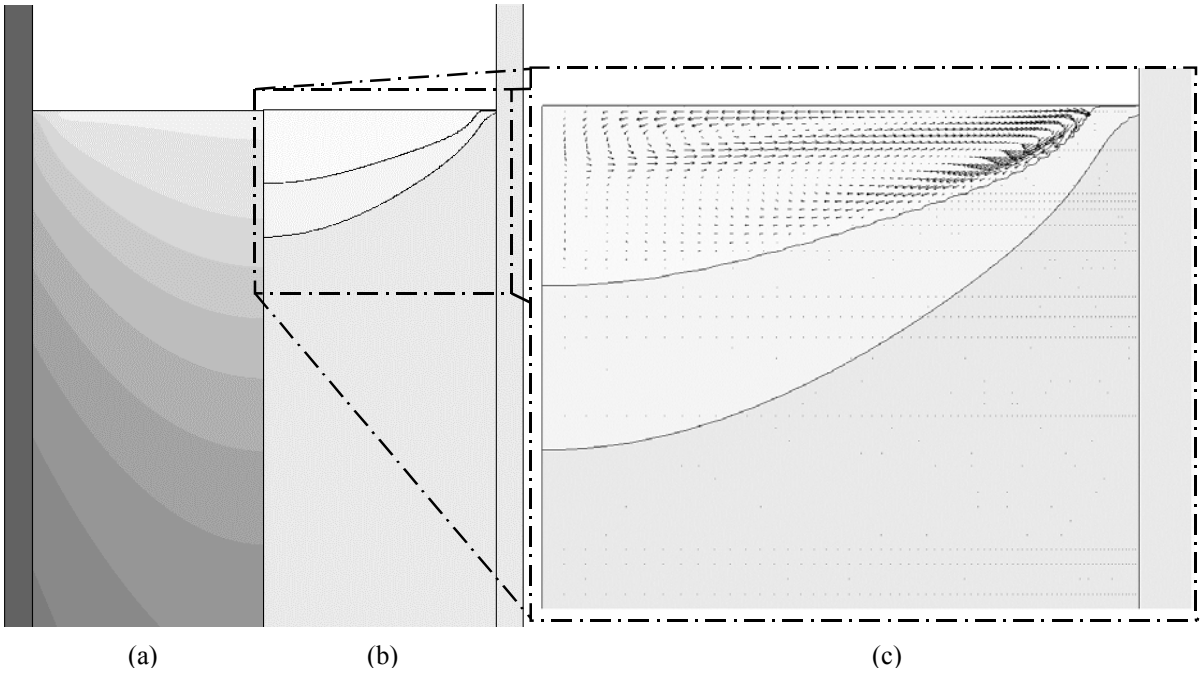

Figure 4: Temperature distribution (a), pool profile (b) and flow pattern (c) of a 510mm ingot simulation (Alloy 718)

A comparison between fluid flow calculated with and without taking into account the magneto-dynamic effects is shown in figure 5. In contrast to the flow conditions described above, the flow in figure 5 (a) only shows one flow regime.

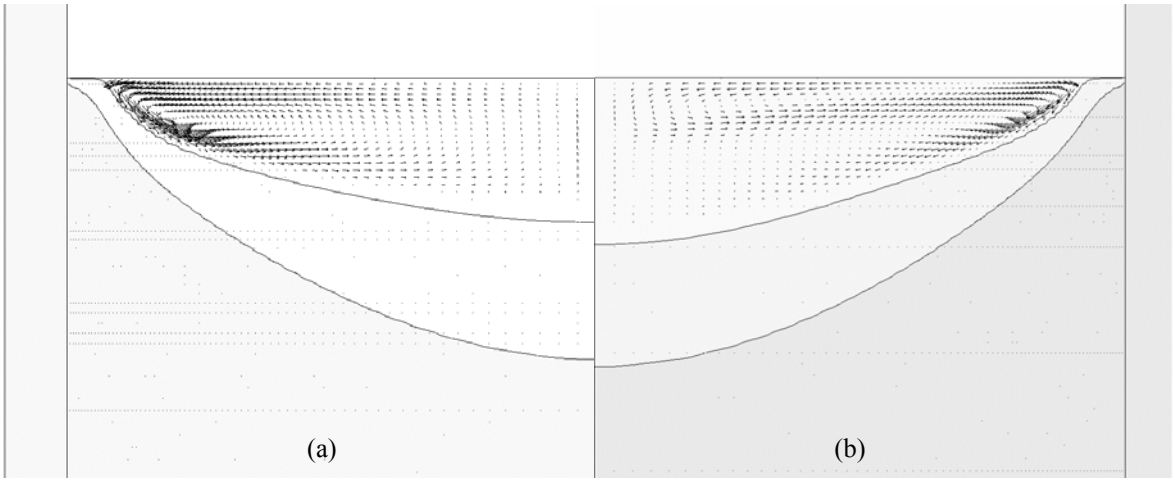

Figure 5: Pool profiles and flow patterns without (a) and with (b) magneto-dynamic effects in 510mm ingots (Alloy 718)

Figure 6 compares the different flow regimes appearing in the 410mm (a) and in the 510mm ingot (b). A decrease in ingot diameter, which can be correlated to a increase in current density, leads to a higher flow velocity in the upper swirl. In addition, the swirl itself gets larger.

4.2 Comparison between measured pool and simulation

The pool profiles of ingots produced at the special steel plant at Böhler Edelstahl GmbH & Co KG in Austria were measured to compare the simulation results with the real pool profiles and to verify the validity of the boundary conditions and assumptions that were made. For this purpose, ingots were made without hot toping and horizontal slices were taken from the top. These slices were etched and the pool profiles were determined from the microstructure, assuming that the transition from columnar to the fine equiaxed grains signifies the solidus line. This is illustrated in Figure 7

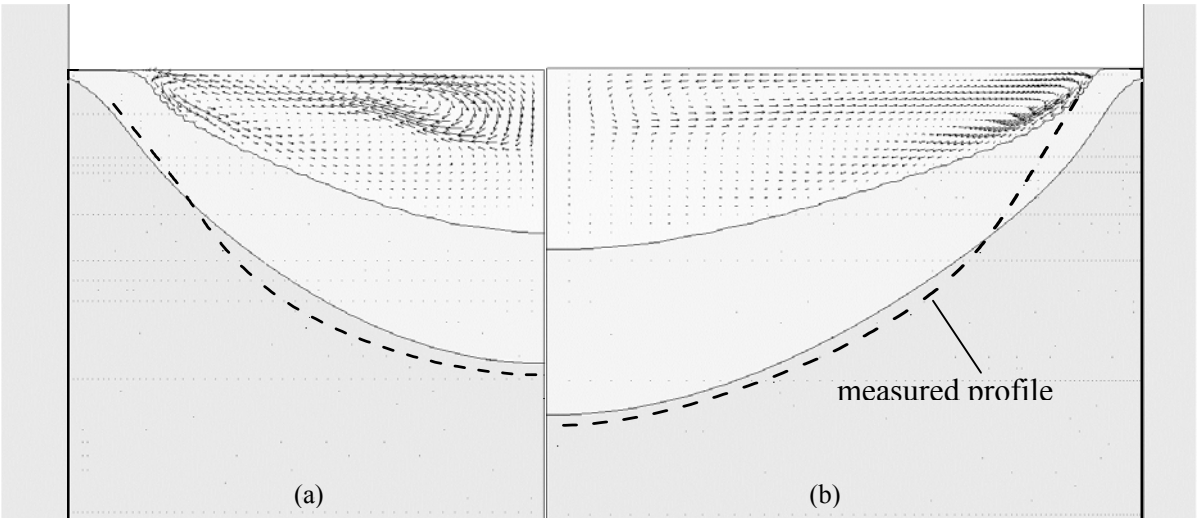

Figure 6: Simulated and measured pool profiles and flow patterns of 410mm (a) and 510mm ingots (b)

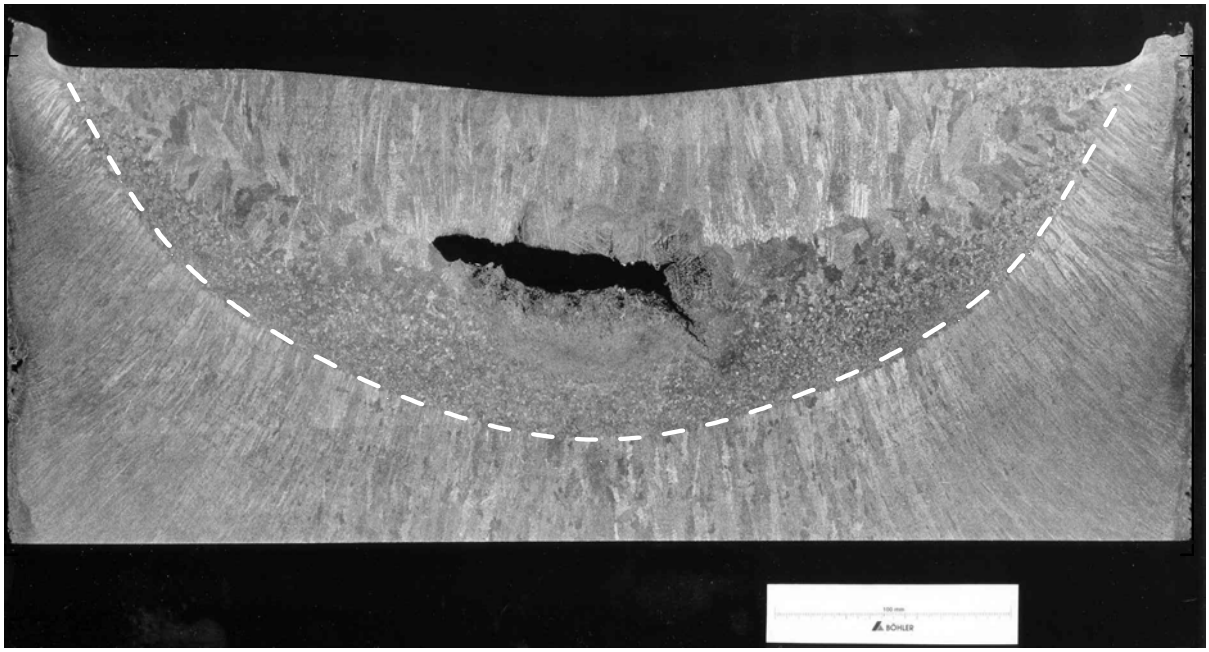

Figure 7: Microstructure and pool profile of a 510 mm ingot remelted without hot topping (Alloy 718).

The comparison between the measured and the calculated pool profile for a 410mm (16") and a 510mm (20") ingot is shown in Figure 6. It should be noted, that the simulated profile of the 410mm ingot (a) quite fits the measured profile; the pool depth of the simulation is nearly equal to that measured. Near to the mould the difference is evident insofar as the slope of the measured solidus line is steeper, ending in the formation of a solid shelf which cannot be simulated accurately. In the inner region of the 510mm ingot (b), the pool depth and the profile of the simulation correlate quite well with the measurement, whereas the difference in the shelf region is a little higher than for the smaller ingot.

5 DISCUSSION AND OUTLOOK

Generally, the calculated temperature distribution and the pool profile agree with typical literature values for the VAR process [10,16,17]. The atypical pool profile near the mould is due to the boundary conditions in the annulus. At this boundary, a liquid layer needs to be established in the program to avoid calculation errors. Various trials have shown that this does not have a large influence on the pool depth or on the flow pattern.

The different flow regimes can be related to the different acting forces (Figure 6): at the top of the pool, where the current density is very high, the flow is mainly driven by Lorentz forces which lead to the flow pattern observed. Further below the surface, the current density decreases and thus the flow regime is mainly driven by buoyancy forces [4,17]. Figure 5 shows the difference between the flow pattern calculated without the magneto-dynamic effects with only buoyancy driven flow, and the flow pattern also taking into account the influence of the Lorentz forces. The higher current density which occurs in the 410mm ingot leads to an increase in Lorentz forces, a larger region of Lorentz driven flow and higher flow velocity.
The comparison between measured and simulated pool profiles indicates that in principal there is a good correlation for both the pool profiles of the 410mm and the 510mm ingot. Furthermore, this shows that the assumption and calculations for the boundary conditions are valid in general and not only "customised" to one dimension.
Some further steps are planned for the future. First, in order to carry out a more accurate validation of the model, a measurement of the local solidification time will be carried out to compare the results with the values derived from the simulation. On this basis, calculations of different parameter sets will be carried out, with the goal of understanding the influence of the various process parameters on the melting behaviour during steady state. Additionally, the simulation will be extended to microstructure and segregation prediction and the simulation of the solidification behaviour of other alloys.

6 REFERENCES

[1] Gmelin Handbook of Inorganic Chemistry, Metallurgy of Iron Vol. 9; Springer Verlag, Berlin 1988
[2] Handbook of vacuum arc science and technology. Edited by R.L. Boxman, D.M. Sanders and P.J. Martin, Noyes Publication, 1995.
[3] Ph. Thévoz, M. Rappaz and J.-L. Desbiolles: 3-MOS: a general FEM code for the prediction of microstructures in castings. In C.M. Bickert ed, Light Metals, pages 975-984, TMS, Warrendale, PA, 1990.
[4] P.A. Davidson, X. He and A.J. Lowe: Flow transition in vacuum arc remelting. Material Science and Technology, 16:699-711, 2000.
[5] A. Jardy and D. Ablitzer: On convective and turbulent heat transfer in VAR ingot pools. In M. Rappaz, M.R. Ozgu and K.W. Mahin eds, Modeling of casting, welding and advanced solidification processes V, pages 699-706, TMS, Warrendale, PA, 1991.
[6] A. Jardy, D. Ablitzer and J.F. Wadier: Magnetohydrodynamic and thermal behavior of electroslag remelting slags, Metall. Trans. B, 22B:111-120, 1991.
[7] P.D. Lee, R. Lothian, L.J. Hobbs and M. McLean: Coupled macro-micro modelling of the secondary melting of turbine disc superalloys. In R.D. Kissinger, D.J. Deye, D.L. Anton, A.D. Cetel, M.V. Nathal, T.M. Pollock and D.A. Woodford, Superalloys, pages 435-442, TMS-AIME, Warrendale, PA, 1996.
[8] X. Xu, W. Zhang and P.D. Lee: Tree ring formation during vacuum arc remelting of INCONEL 718: Part II. Mathematical modeling. Metall. Mater. Trans. A, 33A:1805-1815, 2002.
[9] J. Rappaz : Calcul de l'induction magnétique générée par des courants axiaux et radiaux en coordonnées cylindriques, Technical report. Ecole Polytechnique Fédérale de Lausanne, July 2002.
[10] F. J. Zanner and L. A. Bertram: Vacuum Arc Remelting – an overview. Proc. 8th Intern. Conf. Vac. Met. Linz 1985, 512-552
[11] A. Jardy, L.Falk and D.Ablitzer: Energy exchange during vacuum arc remelting. Ironmakung and Steelmaking Vol. 19 (1992); 226 – 232
[12] K.-O. Yu : Comparison of ESR-VAR processes – part 1 heat transfer characteristics of crucible. Proc. 8th Intern. Conf. Vac. Met. Linz 1985, 512-552
[13] E. H. Kennard: Kinetic Theory of Gases, McGraw-Hill Book Company Inc., 1938, pp. 311-327.
[14] F. Keith: Principles of Heat Transfer. International Text Book Company, 1962.
[15] http://metalcasting.auburn.edu/data/data.htm
[16] F. J. Zanner, R. L. Williamson and R. Harrison: Relationship between 520mm diameter Inconel 718 alloy ingot pool progiles and vacuum arc remellt operational parameters. Special Melting and Processing Technologies, 551 - 563
[17] F. J. Zanner et al: Vacuum arc remelting of Alloy 718. Superalloy 1989 – Metallurgy and Applications; The Minerals, Metals and Materials Society, 1989